Design of Oil-Free Turbocompressors for a Two-Stage Industrial Heat Pump under Variable Operating Conditions

Adeel JAVED[1*], Cordin ARPAGAUS[2], Stefan BERTSCH[2], Jürg SCHIFFMANN[1],

[1] Laboratory for Applied Mechanical Design (LAMD)
École Polytechnique Fédérale de Lausanne (EPFL)
Rue de la Maladière 71b
Neuchâtel 2002, Switzerland

[2] NTB University of Applied Sciences and Technology Buchs
Institute of Energy Systems
Werdenbergstrasse 4
9471 Buchs, Switzerland

* Corresponding Author, E-mail: adeel.javed@epfl.ch

ABSTRACT

A pair of mechanically driven small-scale turbocompressors running on gas lubricated bearings have been designed for a two-stage heat pump application functioning under variable operating conditions. Novelty in the present two-stage heat pump system lies in the application of oil-free turbocompressor technology and the introduction of unused secondary heat from various sources. Managing the operational deviations and the secondary heat during off-design heat pump operation is challenging for the turbocompressors. The turbocompressors can potentially exceed their operating range defined by the surge and choke margins, and the maximum rotational speed limit set by the structural and rotordynamic considerations. A wide operating range is, therefore, a prerequisite design condition for the turbocompressors. The present paper will guide the readers through different stages of the design process of such turbocompressors subjected to various operational and design constraints. Moreover, a stochastic evaluation on the influence of variable operating conditions on the heat pump off-design performance will be detailed.

1. INTRODUCTION

1.1 Motivation

Heat pumps have been identified as a key technology for reducing the exergy losses as compared to conventional boiler systems (Favrat et al., 2008). One of the significant developments has been the realization of multi-stage heat pumps (Favrat et al., 1997; Zehnder, 2004). Studies have shown that domestic-scale multi-stage heat pumps are feasible and achieve higher coefficient of performance (COP) than single-stage types, but suffer from oil migration issues. Subsequently, a comprehensive design and experimental investigation of an oil-free gas bearing supported turbocompressor unit for a domestic two-stage heat pump has been made (Schiffmann & Favrat, 2009; Schiffmann, 2013, 2015). The turbocompressor has seen application as a compressor-turbine unit in the experimental investigation of a thermally driven heat pump cycle with promising results (Demierre et al., 2014).

In this paper, a 6.5kW two-stage heat pump concept driven by oil-free turbocompressors with two heat sources at different temperature levels is proposed for decentralized domestic application (Granwehr & Bertsch, 2012; Arpagaus et al., 2016). A secondary heat from different unused sources such as waste heat, liquid from cooling circuits or process steam has been added to the thermodynamic cycle to increase the COP. Figure 1 illustrates the thermodynamic cycle of the heat pump concept along with various operating conditions and their expected deviations. As the heat pump shifts to an off-design operating condition, the turbocompressors can potentially surge or choke depending on the magnitude of deviations and the secondary heat. Hence, miniature turbocompressors designed for wide operating range satisfying the manufacturing and assembly constraints are necessary for this application.

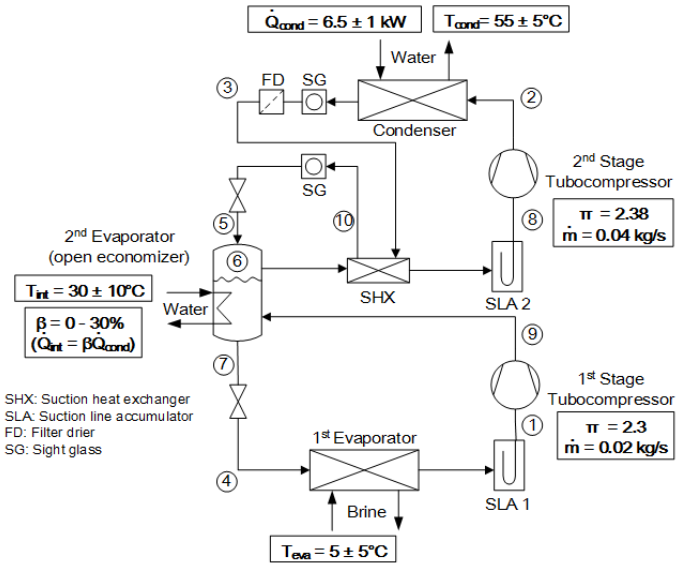

Figure 1: Schematic diagram of the two-stage heat pump cycle

1.2 Goals and Objectives

The goal of this study is to achieve viable turbocompressor designs by using a mix of 1D and 3D design methods. The main objectives are: (1) define the compressor specifications, (2) assess the effects of operational uncertainties on the heat pump performance, and (3) devise unified design guidelines for optimum impeller blading design.

1.3 Scope of the Paper

A comprehensive methodology has been applied to design the turbocompressors. An in-house Matlab based two-stage heat pump model has been used to calculate the steady-state system performance for the given operating conditions with 20% β secondary heat. The model calls the real gas refrigerant database Refprop (Lemmon et al., 2002) to estimate the R134a refrigerant fluid properties. A 1D centrifugal compressor design has been made based on the heat pump requirements. The 1D design specifies the preliminary geometry and performance maps of the two turbocompressor stages. The 1D maps are then integrated in the heat pump model to simulate off-design heat pump operation. A stochastic evaluation using the Monte Carlo method has been made to estimate the heat pump performance statistics under operational deviations. Finally, a 3D impeller blading optimization is performed using comprehensive CFD modeling. The influence of blading on the compressor fluid physics is studied and a design guideline is presented.

2. 1D TURBOCOMPRESSOR DESIGN

The turbocompressor design process begins with 1D meanline modeling of different components as illustrated in Fig 2. A commercial 1D model COMPAL ® from Concepts NREC has been used. The model is based on the two-zone methodology (Dean, 1974; Japikse, 1985, 1996). The design process begins at the inducer (station 1), proceeds to the exducer with primary zone, secondary zone and mixed-out state calculations, and then to the stationary components comprising a vaneless diffuser (station 5) and the discharge volute (station 6 and 7).

2.1 Design Selections

A set of inputs is required during the design process. Selection of these inputs is based on designer's experience, performance requirements and any design constraints.

Rotational speed selection: The $n_s d_s$ diagram for single stage compressors (Balje, 1981) has been used to obtain a conservative estimate of the turbocompressor rotational speed at design point. The maximum rotational speed and transmission torque are limited to 280,000 rpm and 45 mNm, respectively. For the first stage turbocompressor, n_s = 0.62

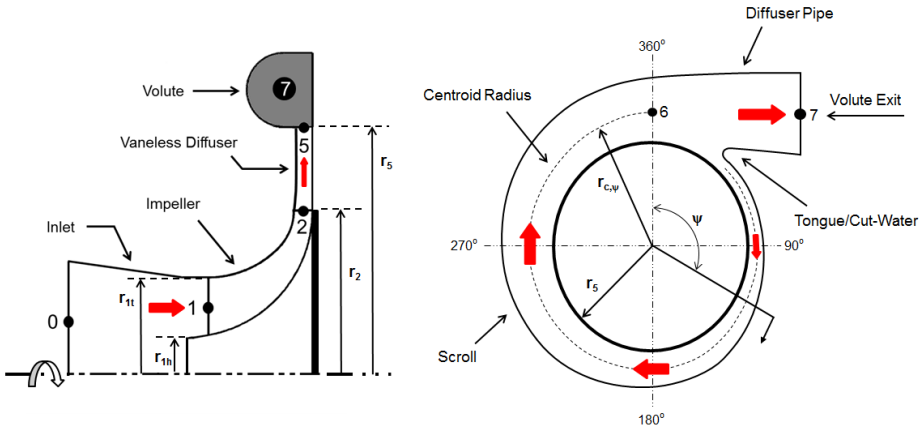

Figure 2: The centrifugal compressor stage and volute with station numbers and main dimensions

has been selected, which complies to the 80% compressor efficiency island for a radial-type compressor. This results in an impeller with 15.2 mm tip diameter with design rotational speed of approximately 227,000 rpm at a torque of 21 mNm. For the second stage turbocompressor, a small trade-off has been made by selecting a comparatively lower specific speed n_s = 0.57 to gain more maximum speed margin. Consequently, an impeller with 14.8 mm tip diameter rotating at approximately 235,000 rpm at a torque of 39 mNm is obtained from 1D calculation at design point.

Inducer design: The impeller will be mounted on a separate titanium shaft fused to the main rotor. Since the shaft can be designed independently of the main rotor and the torque transmission is well within the torsional rigidity limit, r_{1h}= 1.5 mm is selected for both turbocompressors following a parametric study.

Blading and tip-clearance: A total of 16 blades have been specified for both turbocompressor impellers with half of the blades allocated to splitter blades. A blade thickness t_b= 0.25 mm is selected considering manufacturability with aluminum. The tip-clearance t_{clr}= 80 μm is defined initially based on the manufacturing and assembly limitations, and bearing clearances with an intention to reduce it in subsequent evaluations.

Exducer design: The two-zone modeling is case-specific in terms of computation of the mass flow distribution between the primary and secondary flow zones represented by the secondary zone mass flux fraction χ (where $\chi = \dot{m}_{sec}/\dot{m}$). Since data is not available for small-scale impellers in the range of 15 mm tip diameter, a value χ = 0.2 has been specified for the 1D designs. The use of blade backsweep β_{2b} extends the compressor operating range, improves impeller exit flow uniformity, and increases the overall pressure recovery in the compressor (Japikse, 1996; Cumpsty, 2004; Hildebrandt & Genrup, 2007). For the turbocompressors, β_{2b} = 45° has been selected. The exducer depth or height b_2 has been defined by the exit swirl parameter $\lambda_{2m} = c_{\theta 2m}/c_{m2m}$ (also a measure of the absolute flow angle $\alpha_{2m} = tan^{-1}\lambda_{2m}$). Following the guideline provided in Japikse (1996), λ_{2m} = 4.0 (α_{2m} = 76°) and λ_{2m} = 4.2 (α_{2m} = 76.6°) have been specified for the first and second stage turbocompressors, respectively. Finally, the diffusion properties in the primary flow zone are estimated from the two-elements-in-series model (TEIS) by defining the effectiveness parameters η_a= 0.4 and η_b= 0.2 suggested for small-scale impellers (Japikse, 1984, 1996).

Vaneless diffuser design: Vaneless diffusers provide a wide operating range. For the impellers having design point exit swirl parameter λ_{2m} in the range of 4.0 ($\alpha_{2m} \approx 76°$), the diffuser is likely to experience a rotating stall triggered by local flow reversal. For wide-range and peak efficiency at design point, λ_{2m} should ideally be approximately 2.0–2.5 (α_{2m} between 63° and 68°) (Japikse, 1996; Jansen, 1964; Johnston & Dean, 1966; Rodgers & Sapiro, 1972). Hence, a frontal pinch is applied to reduce the diffuser swirl to a more desirable value. For the first stage turbocompressor, the front pinch reduces the exit height of the vaneless diffuser b_5 to 0.65 times the impeller exit height b_2 (b_5/b_2 = 0.65) resulting in λ_5 = 2.25 (α_5 = 66°) at diffuser exit. For the second stage turbocompressor, the front pinch reduces the exit height of the vaneless diffuser b_5 to 0.8 times the impeller exit height b_2 (b_5/b_2 = 0.8) resulting in λ_5 = 2.9 (α_5 = 71°) at diffuser exit. Both diffusers have the exit radius r_5 located at 1.65 times the impeller exit radius r_2 (r_5/r_2 = 1.65), while the pinch is located at about 1.1 times the impeller exit radius r_2 (r_{pinch}/r_2 = 1.1).

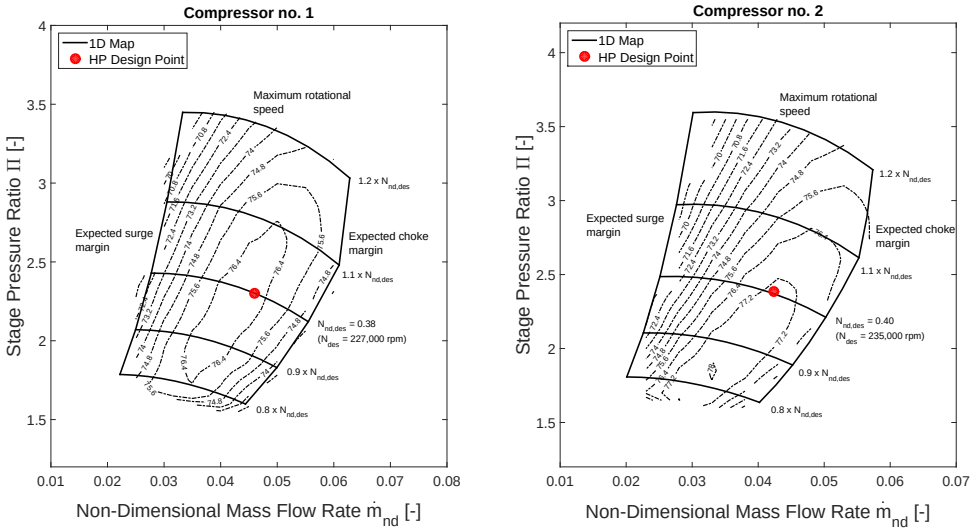

Figure 3: 1D compressor maps for first and second stage turbocompressors with isentropic efficiency contours

Volute design: An external overhung volute design with machined tunnel-type cross-sections has been opted for the two turbocompressors. The cross-sectional areas A_ψ at different azimuth angles ψ have been sized following a simple correlation derived from the principles of angular momentum and mass conservation as $A_\psi = \psi \times SP \times \frac{r_{c,\psi} b_5}{\lambda_5}$. Here SP represents the sizing parameter used to scale the volute through an iterative procedure, $SP = 0.85$ has been found to be an appropriate scale for both turbocompressors to maintain almost constant $c_{\theta 5} \approx c_6$ at design point.

2.2 1D Turbocompressor Performance

Following the extensive design exercise, 1D designs are obtained for the two turbocompressor stages. Table 1 compiles the main compressor geometric and the design point performance data. Considering the geometry, the two turbocompressors will be one of the smallest of their kind with tip diameters d_2 in order of 15 mm once manufactured and tested. Despite their small size and relatively large tip-clearance (relative tip-clearance $\varepsilon = t_{clr}/b_2$ is approximately 13–15%), the compressors are able to achieve a healthy isentropic efficiency in the range of 77% at design point. Off-design performance is equally important for the turbocompressors. Therefore, non-dimensionalized 1D performance maps have been obtained, as shown in Fig. 3. By converting the compressor performance to non-dimensional rotational speed $N_{nd} = Nd_2/a_{00}$ and non-dimensional mass flow rate $\dot{m}_{nd} = \dot{m}/(\rho_{00} a_{00} d_2^2)$, the influence of varying inlet conditions with a real gas is removed (Dixon, 2005). Empirical stall checks provided in the 1D design tool for different stage components have been monitored at low mass flow rate operations. Considering the stable operating range $R = \frac{\dot{m}_{choke} - \dot{m}_{surge}}{\dot{m}_{choke}}$ at design rotational speed, the two turbocompressors are in a relatively high range category with R reaching 50% for moderately low flow coefficient compressors having a design pressure ratio around 2.3–2.5 (Japikse, 1996).

2.3 Off-Design Heat Pump Performance Evaluation

The 1D compressor performance maps for the two turbocompressor stages are primarily used to interpolate of isentropic efficiencies at heat pump off-design operating conditions by using the triangulation-based scattered interpolation func-

Table 1: Geometric specifications and design point performance calculated by the 1D meanline model

Parameter	Compressor no. 1	Compressor no. 2
Inducer shroud radius, r_{1t} (mm)	3.62	3.43
Tip radius (diameter), r_2 (d_2) (mm)	7.62 (15.2)	7.4 (14.8)
Tip height, b_2 (mm)	0.62	0.53
Tip-clearance (relative), t_{clr} (ε) (mm)	0.08 (13%)	0.08 (15%)
Blade angle at inducer tip, β_{1b} (deg)	57°	57°
Backsweep angle, β_{2b} (deg)	45°	45°
Diffuser radius, r_5 (mm)	12.57	12.22
Diffuser height, b_5 (mm)	0.405	0.42

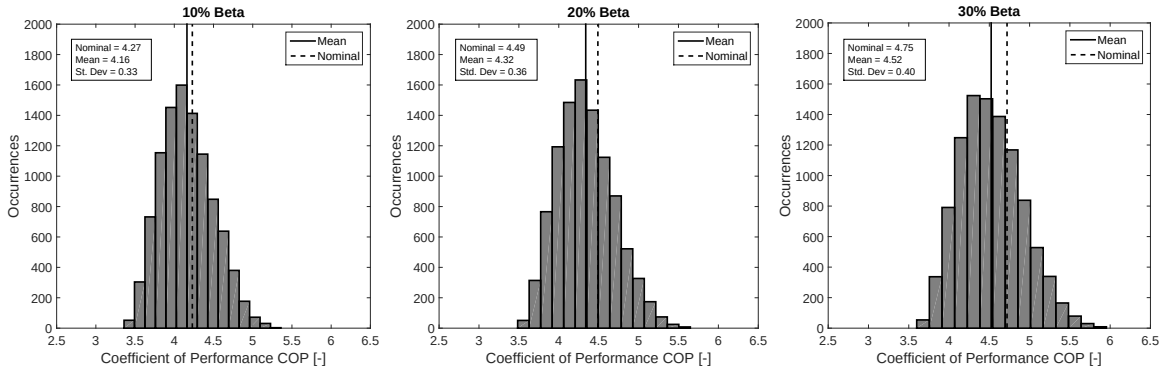

Figure 4: Heat pump performance under deviations in operating conditions

tion provided in Matlab. The method is efficient and particularly advantageous due to its extrapolation functionality (Amidror, 2002). A total of 10,000 Monte Carlo samples of uniformly distributed random input parameter variations have been simulated with the heat pump model. The heat pump input parameters and their respective deviations are summarized in Table. 2. Two assumptions have been made during the stochastic evaluation: (1) the temperature drops across source and sink fluid streams are kept constant by adjusting their respective mass flow rates for more stable regulation of pressures in the heat exchangers, and (2) the turbocompressors are able to operate beyond their expected operating ranges (data is thus extrapolated) since the actual operating ranges are not known at this point. These aspects will be studied in more detail during the experimental phase.

The off-design performance of the two-stage heat pump is statistically summarized as COP probability distributions in Fig. 4 for different β levels. The nominal COP increases by 10% from 4.27 to 4.75, while the mean COP increases by 8% from 4.16 to 4.52 with 10-30% β second source heat addition. Furthermore, the COP standard deviation increases from 0.33 to 0.40. Note that the mean COP levels are actually lower than the nominal COP levels, thereby indicating a systematic heat pump performance shift under stochastic input parameter deviations. This systematic shift also increases in magnitude with increase in β levels.

3. 3D COMPRESSOR IMPELLER DESIGN

Many important analytical and experimental studies have been made to quantify the flow field in centrifugal compressors (Johnson, 1978; Eckardt, 1975, 1976; Krain, 1981; Hirsch et al., 1996; Casey et al., 1992). According to these studies, the flow field in a centrifugal compressor stage is highly complex and subjected to local accelerations due to centrifugal forces (curvature effect) and Coriolis forces (rotational effect). The resulting pressure gradients generate secondary flow in shape of streamline vorticity along the end-walls (hub and shroud surfaces) from pressure side (PS) to the suction side (SS) due to blade-to-blade curvature, secondary flow along the blade surfaces (span-wise direction) due to meridional curvature, and the secondary flow generated by the Coriolis forces mainly in the radial parts of the impeller. The tip-leakage flow due to migration of high pressure flow from PS to SS of the blades through the tip-clearance gap supplements the secondary zone by forming a large vortex that stretches stream-wise in the blade passages causing a considerable performance loss. An appropriate 3D impeller blade design suppressing the secondary and tip-leakage flow is, therefore, very important. An observation based approach has been applied to design the turbocompressor impellers using steady-state CFD modeling with Ansys CFX. Note that the first stage turbocompressor impeller has been optimized. Similar blading is to be applied for the second stage turbocompressor impeller.

Table 2: Heat pump operating parameters and their deviations

Parameter	Nominal	Deviation
1^{st} source temperature, T_{eva} [°C]	5	±5
2^{nd} source temperature, T_{int} [°C]	30	±10
Sink temperature, T_{cond} [°C]	55	±5
Condenser heating capacity, $\dot{Q}_{cond}$ [kW]	6.5	±1
2^{nd} source heat capacity, $\dot{Q}_{int}$ [kW]	10-30% β	±0.5

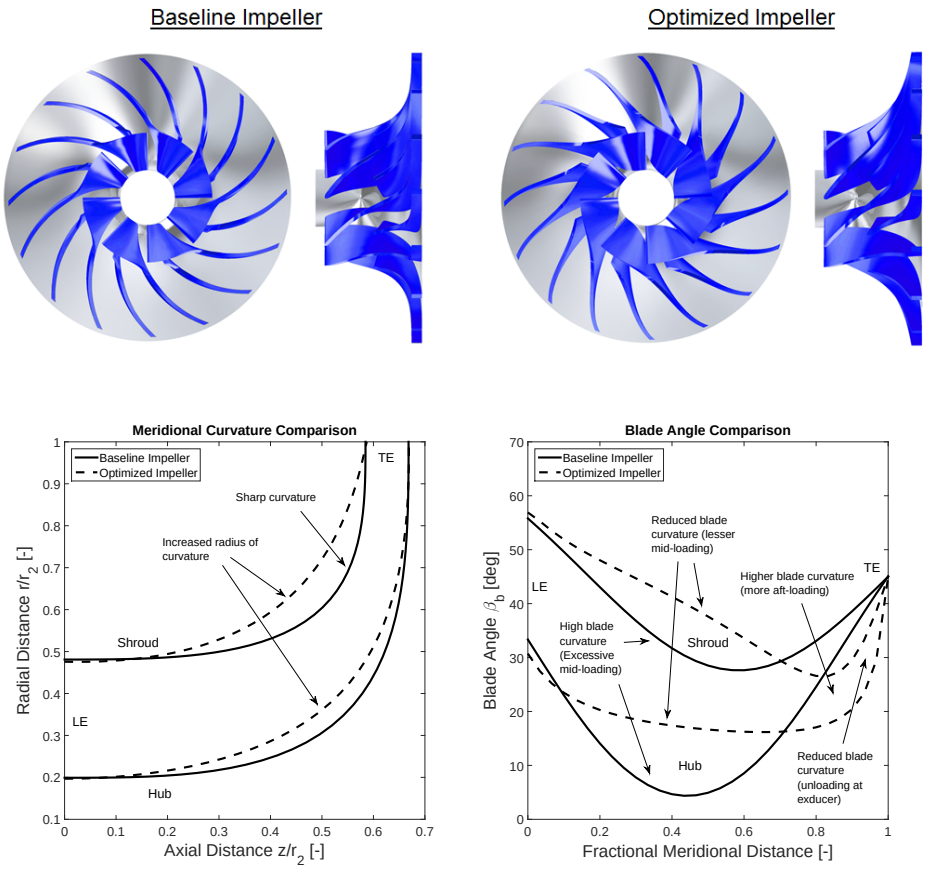

Figure 5: Comparison between the baseline and the optimized impeller blade designs

3.1 CFD Setup

The following steps have been taken to set up an appropriate CFD model of the turbocompressor stage:

3D geometric model: The 1D geometric data has been used to construct a 3D geometric model using ANSYS BladeGen. The model consists of a straight inlet duct, impeller and the vaneless diffuser in a single passage fluid domain. The impeller meridional hub and shroud profiles, and blade shape have been defined by Bézier curves of 5^{th} order (six control points). The splitter blades begin from a meridional distance of approximately 40% from the leading edge (LE) and follow the blade angle and thickness distributions of the full blades till the trailing edge (TE). Note that the volute is not included in the present CFD study to reduce the computational cost.

Grid processing: A 3D structured grid has been created using the H-Grid and O-Grid topologies in ANSYS TurboGrid. The tip-clearance gap is also introduced in the grid processing tool by trimming down the impeller shroud profile. A grid independence study has been made by simulating three different grid sizes containing 0.28 million, 1.2 million and 4.0 million hexahedral elements at design point. The grid with 1.2 million elements is found to be a suitable choice by comparing compressor pressure ratio and isentropic efficiency convergence with increase in grid size.

Solver setup: Since a single passage domain simulation is considered, the symmetric surfaces are defined as periodic boundaries. The interfaces between the inlet duct, impeller and the vaneless diffuser are defined as stage/mixing plane. All the wetted surfaces have been considered as hydraulically smooth; hence surface roughness is not defined and skin friction loss is only caused by fluid viscosity. The total inlet conditions have been defined at the inlet boundary, while design mass flow rate is defined at the outlet boundary of the domain. Refrigerant fluid R134a has been set as the fluid medium. The k-ω Shear Stress Transport (SST) turbulence model (Menter, 1993) has been specified for all the CFD analyses.

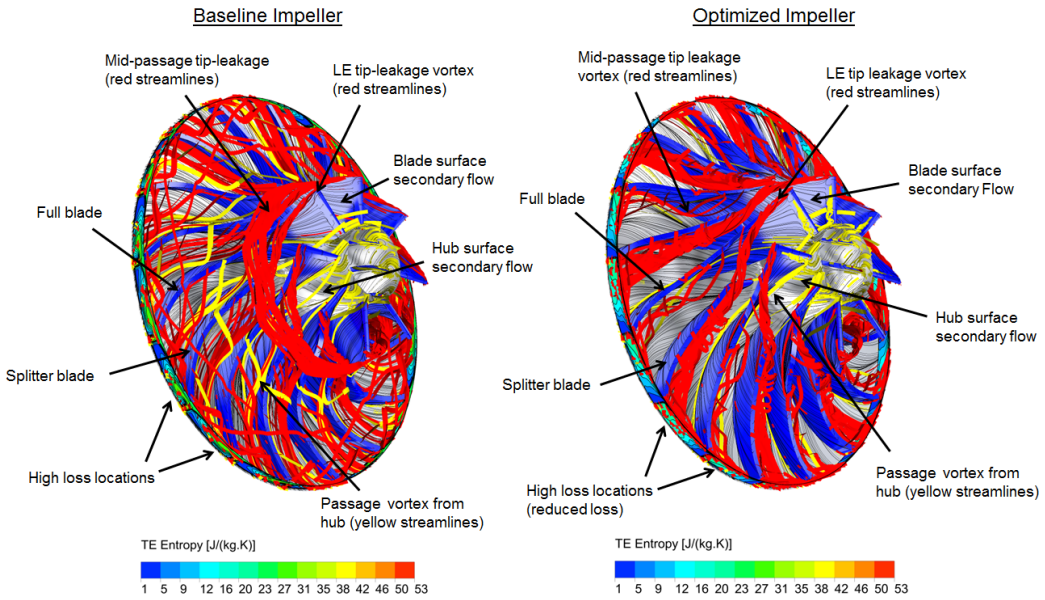

Figure 6: Comparison of secondary and tip-leakage flow between the baseline and optimized impeller designs

3.2 Methodology for optimized blade design

Although each impeller design is a new problem, a good blade passage can be designed by controlling the meridional and blade-to-blade curvatures in order to have a uniform velocity or pressure distribution in the blade passages, thus reducing the secondary and tip-leakage flows. Figure 5 compares the baseline and optimized impeller geometries in detail. Following steps have been taken to iteratively optimize the impeller design:

- The excessive meridional curvature has been reduced at the hub and shroud to have a more circular axial-to-radial bend. The small inducer hub diameter facilitates the design of a smooth circular channel.
- The mean blade loading, generally defined as blade-to-blade loading coefficient $\Lambda = \frac{w_{ss}-w_{ps}}{\bar{w}}$ (where $\bar{w} = \frac{w_{ss}+w_{ps}}{2}$), has been reduced in the middle section of the impeller passages by reducing the blade curvature (approximately 10° higher mean blade angle compared to the baseline impeller). Furthermore, the blade curvature is maximum between 60% and 80% of the passage length, which ensures an aft-loaded blading.
- The influence of Coriolis force (dominant in the radial part of the impeller) has been reduced by unloading the exducer through lowering the blade curvature from 80% of the passage length till the TE of the impeller.
- The splitter blades further helps in reducing the average loading per blade and reduce the tip-leakage flow.

The end result is a more organized impeller design with smoother blade passages compared to the baseline impeller.

3.3 Internal flow comparison

Figure 6 presents a detailed picture of the tip-leakage flow for the baseline and optimized impeller designs. Looking at the baseline impeller flow field, the blade passages are engulfed with large amount of vorticity originating mainly from the tip-leakage flow. A large tip-leakage vortex initiates from the LE shroud, which moves towards the splitter blade SS and stretches to the TE forming a large loss region indicated by the TE entropy contours. Due to high mid-loading, an excessive tip-leakage also appears and swirls in the mid-passage region. Fig. 6 also shows the end-wall and blade surface secondary flows. As expected, the secondary flow moves from the PS to SS across the hub surface (blade-to-blade) and span-wise from hub to shroud. In comparison, the optimized impeller shows an improved vorticity structure in the blade passages. Similar to the baseline impeller, the tip-leakage initiates at the LE shroud and propagates to the splitter blade SS mixing with the tip-leakage flow originating from the splitter blade. Unlike the baseline impeller, this tip-leakage vortex is more aligned with the SS of the splitter blades. Some more leakage flow is seen in the aft-sections of the blade passages. Overall, the flow field contains lesser vorticity, which results in a more uniform flow and lesser entropy production at the TE compared to the baseline impeller. The end-wall and blade surface secondary flows

appear to be improved slightly. However, it is extremely challenging to control the secondary flow in the presence of large tip-leakage flow. A more detailed survey is required in this case.

3.4 Overall performance comparison

With an improvement in the flow field, the design point performance also increased significantly for the optimized impeller compared to the baseline. The pressure ratio increased by approximately 15% from 2.13 to 2.48, while isentropic efficiency increased by 3.5% points from 76% to 79.5%. Furthermore, approximately 16% higher choke mass flow rate then the 1D model prediction is expected from the optimized compressor design, thus increasing the compressor operating range R to almost 57% at the design rotational speed.

4. CONCLUSIONS

The following conclusions are drawn from this study:

- The stochastic performance evaluation exposes the difference between nominal heat pump performance and the performance under deviating operating conditions. An integrated heat pump and 1D design optimization could be studied, where the system is robustly designed for maximizing the compressor operating range and heat pump performance in general.
- Smaller inducer hub diameter improves the impeller and overall compressor performance by allowing a lower relative velocity at the tip. The blade design can also benefit from a more circular channel and thus improved passage flow.
- For a wide operating range, a careful balance between the work transfer in the impeller and vaneless diffuser performance is necessary. A pinched vaneless diffuser can improve the work transfer in the impeller, while allowing the diffuser to operate stably at off-design conditions.
- For small-scale compressors, the large tip-clearance ($\varepsilon > 5\%$) and the associated tip-leakage flow dominate the overall flow field in the impeller passages. A moderate blade loading and more aft-loaded distribution is found to be most favorable in the present case.
- Miniature inlet guide vanes and low-solidity vaned diffusers could be studied in a future project to enhance the operating range and peak efficiency of the first stage turbocompressor.

NOMENCLATURE

a	speed of sound	(m/s)
A	area	(mm^2)
b	height or width	(mm)
c	absolute velocity	(m/s)
d	diameter	(mm)
d_s	specific diameter	(-)
$\dot{m}$	mass flow rate	(kg/s)
n_s	specific speed	(-)
N	rotational speed	(rpm)
$\dot{Q}$	heat capacity	(kW)
r	radius	(mm)
R	range	(-)
SP	sizing parameter	(-)
t	thickness/tip-clearance	(mm/mm)
T	temperature	(K)
w	relative velocity	(m/s)
z	axial distance	(mm)
α	absolute angle from the meridional axis	(deg)
β	secondary heat fraction/relative angle from the meridional axis	(-/deg)
χ	secondary mass flux fraction	(-)

ε	relative tip-clearance	(-)
η	effciency	(%)
λ	swirl parameter	(-)
Λ	blade loading coefficient	(-)
ρ	density	(kg/m^3)
Π	pressure ratio	(-)
ψ	azimuthal angle	(deg)

Subscripts

b	blade
c	centroid
clr	clearance
cond	condenser
des	design
eva	evaporator
h	hub
int	intermediate
m	meridional/mixed-out
nd	non-dimensional
t	tip
θ	tangential

Subscript

$\bar{}$	average or mean value

REFERENCES

Amidror, I. (2002). Scattered data interpolation methods for electronic imaging systems: A survey. *Journal of Electronic Imaging*, *11(2)*, 157-176.

Arpagaus, C., Bertsch, S., Javed, A., & Schiffmann, J. (2016). Two-stage heat pump using oil-free turbocompressors–system design and simulation. In *Proceedings of 16th international refrigeration and air conditioning conference* (pp. 1–10). Purdue, USA: Paper ID 2101.

Balje, O. (1981). *Turbomachines, a guide to design, selection and theory*. John Wiley & Sons.

Casey, M., Dalbert, P., & Roth, P. (1992). The use of 3d viscous flow calculations in the design and analysis of industrial centrifugal compressors. *ASME Journal of Turbomachinery*, *114*, 27–37.

Cumpsty, N. (2004). *Compressor aerodynamics*. Krieger Drive, Malabar, Florida 32950: Krieger Publishing Company.

Dean, R. (1974). *The fluid dynamic design of advanced centrifugal compressors* (Lecture Series). Von Karman Institute for Fluid Dynamics (VKI).

Demierre, J., Favrat, D., Schiffmann, J., & Wegele, J. (2014). Experimental investigation of a thermally driven heat pump based on a double organic cycle and an oil-free compressor-turbine unit. *International Journal of Refrigeration*, *44*, 91–100. doi: 10.1016/j.ijrefrig.2014.04.024

Dixon, S. (2005). *Fluid mechanics, thermodynamics of turbomachinery*. Oxford, UK: Elsevier Inc.

Eckardt, D. (1975). Measurements in the jet-wake discharge flow of a centrifugal compressor impeller. *ASME Journal of Engineering for Power*, *97(3)*, 337–346.

Eckardt, D. (1976). Detailed flow investigations within a high speed centrifugal compressor impeller. *Journal of Fluids Engineering*, 390–402.

Favrat, D., Marechal, F., & Epelly, O. (2008). The challange of introducing an exergy indicator in a local law on energy. *Journal of Energy*, *33*, 130–136. doi: 10.1016/j.energy.2007.10.012

Favrat, D., Nidegger, D., Reymond, D., & Courtin, G. (1997). Comparison between a single-stage and a two-stage air to water domestic heat pump with on variable speed compressor. In *Proceedings of the iir conference on heat pump systems, energy efficiency and global warming.* Linz, Austria.

Granwehr, E., & Bertsch, S. (2012). *Heat pump* (Patent No. WO 2012/040864 A1).

Hildebrandt, A., & Genrup, A. (2007). Numerical investigation of the effect of different back sweep angle and exducer width on the impeller outlet flow pattern of a centrifugal compressor with vaneless diffuser. *ASME Journal of Turbomachinery*, *129*, 421–433. doi: 10.1115/1.2447873

Hirsch, C., Kang, S., & Pointel, G. (1996). A numerically supported investigation of the 3d flow in centrifugal impellers - part ii: Secondary flow structure. In *Proceedings of asme international gas turbine and aeroengine congress and exhibition.* Birmingham, UK: 96-GT-152.

Jansen, W. (1964). Rotating stall in a radial vaneless diffuser. *ASME Journal of Basic Engineering*, *119*, 750–758.

Japikse, D. (1984). A critical evaluation of stall concepts for centrifugal compressors and pumps - studies in component performance part 7. In *Proceedings of asme winter annual meeting.* New Orleans, USA: American Society of Mechanical Engineers (ASME).

Japikse, D. (1985). Assessment of single- and two-zone modeling of centrifugal compressors. studies in component performance: Part 3. In *Proceedings of gas turbine conference and exhibit.* Houston, Texas, USA.

Japikse, D. (1996). *Centrifugal compressor design and performance*. Concepts ETI.

Johnson, M. (1978). Secondary flow in rotating bends. *ASME Journal of Engineering for Power*, *100*, 553–560.

Johnston, J., & Dean, J., R.C. (1966). Losses in vaneless diffusers of centrifugal compressors and pumps. *ASME Journal of Engineering for Power*, 49–60.

Krain, H. (1981). A study on centrifugal impeller and diffuser flow. *ASME Journal of Engineering for Power*, *103*, 688–697.

Lemmon, E., McLinden, M., & Huber, M. (2002). *Nist reference fluid thermodynamic and transport properties* (NIST Standard Reference Database No. 23). National Institute of Standards and Technology.

Menter, F. R. (1993). Zonal two-equations k-ω turbulence models for aerodynamic flows. In *Proceedings of the aiaa 24th fluid dynamics conference.* Orlando, Florida, USA: AIAA 93-2906.

Rodgers, C., & Sapiro, L. (1972). Design considerations for high-pressure-ratio centrifugal compressors. In *Proceedings of asme gas turbine and fluids engineering conference.* San Francisco, USA: 72-GT-91.

Schiffmann, J. (2013). Enhanced groove geometry for herringbone grooved journal bearings. *Journal of Engineering for Gas Turbines and Power*, *135*(10), 102501-1–102501-8. doi: 10.1115/1.4025035

Schiffmann, J. (2015). Integrated design and multi-objective optimization of a single stage heat-pump turbocompressor. *Journal of Turbomachinery*, *137*, 071002-1–071002-9. doi: 10.1115/1.4029123

Schiffmann, J., & Favrat, D. (2009). Experimental investigation of a direct driven radial compressor for domestic heat pumps. *International Journal of Refrigeration*, *32*, 1918–1928. doi: 10.1016/j.ijrefig.2009.07.006

Zehnder, M. (2004). *Efficient air–water heat pumps for high temperature lift residential heating, including oil migration aspects*. École Polytechnique Fédérale de Lausanne (EPFL).

ACKNOWLEDGMENT

The authors would like to thank the Swiss Competence Center for Energy Research on Efficiency of Industrial Processes (SCCER EIP) and the Swiss Federal Office for Energy (SFOE) for their financial support, and Prof. Michael Casey and Dr. Daniel Rusch for their useful discussions and insights.